nature communications

Article

https://doi.org/10.1038/s41467-024-54114-3

Giant tunnel electroresistance through a Van der Waals junction by external ferroelectric polarization

Received: 23 July 2024

Accepted: 2 November 2024

Published online: 09 November 2024

Check for updates

Guangdi Feng[1,2,3,6], Yifei Liu[1,2,6], Qiuxiang Zhu[1,2,6], Zhenyu Feng[1,2], Shengwen Luo[1,2], Cuijie Qin[1,2], Luqiu Chen[1,2], Yu Xu[1,2], Haonan Wang[1,2], Muhammad Zubair[1,2], Ke Qu[1,2], Chang Yang[1,2], Shenglan Hao[1,2], Fangyu Yue[1,2], Chungang Duan[1,2,4], Junhao Chu[1,2,5] & Bobo Tian[1,2,3]

The burgeoning interest in two-dimensional semiconductors stems from their potential as ultrathin platforms for next-generation transistors. Nonetheless, there persist formidable challenges in fully obtaining high-performance complementary logic components and the underlying mechanisms for the polarity modulation of transistors are not yet fully understood. Here, we exploit both ferroelectric domain-based nonvolatile modulation of Fermi level in transitional metal dichalcogenides (MoS_2) and quantum tunneling through nanoscale hexagonal boron nitride (h-BN). Our prototype devices, termed as vertical tunneling ferroelectric field-effect transistor, utilizes a Van der Waals MoS_2/h-BN/metal tunnel junction as the channel. The Fermi level of MoS_2 is bipolarly tuned by ferroelectric domains and sensitively detected by the direct quantum tunneling strength across the junction, demonstrating an impressive electroresistance ratio of up to 10^9 in the vertical tunneling ferroelectric field-effect transistor. It consumes only 0.16 fJ of energy to open a ratio window exceeding 10^4. This work not only validates the effectiveness of tailored tunnel barriers in manipulating electronic flow but also highlights a new avenue for the design flexibility and functional versatility of advanced ferroelectric memory technology.

The MOSFETs (Metal-Oxide-Semiconductor Field-Effect Transistors) undeniably serve as the foundational building blocks of the contemporary information society, playing an indispensable role in the realm of microelectronics. Although silicon-based MOSFET has made significant progress over the past few decades, successfully advancing to the sub-10 nm process level, continuous miniaturization is facing challenges due to physical limitations and technical obstacles, such as increased leakage current, power control issues, and manufacturing costs[1]. To overcome these existing bottlenecks, both the scientific community and the commercial industry are exploring novel materials and technologies. Two-dimensional (2D) semiconductors, with their unique layered van der Waals architecture, absence of interlayer binding constraints, and remarkable mechanical resilience, have emerged as highly promising candidates for next-generation semiconductor technology. These materials offer precise atomic-level

[1]Key Laboratory of Polar Materials and Devices, Ministry of Education, Department of Electronics, East China Normal University, Shanghai 200241, China. [2]Shanghai Center of Brain-inspired Intelligent Materials and Devices, Shanghai 200241, China. [3]Chongqing Key Laboratory of Precision Optics, Chongqing Institute of East China Normal University, Chongqing 401120, China. [4]Collaborative Innovation Center of Extreme Optics, Shanxi University, Shanxi 030006, China. [5]Institute of Optoelectronics, Fudan University, Shanghai 200433, China. [6]These authors contributed equally: Guangdi Feng, Yifei Liu, Qiuxiang Zhu. e-mail: qxzhu@clpm.ecnu.edu.cn; bbtian@ee.ecnu.edu.cn

control opportunities that can improve integration capabilities, reduce power consumption, and enhance device performance[2–5].

MoS_2 stands out as one of the extensively investigated 2D semiconductors due to its exceptional properties, boasting well-defined bandgap, stability in ambient conditions, and relatively high charge carrier mobility[6]. These unique attributes position MoS_2 at the forefront of modern electronics and optoelectronics, encompassing memories and photodetectors based on field-effect transistors (FETs)[7,8]. Significant progress has been made in the research of MoS_2 FETs. Radisavljevic et al. fabricated a planar FET based on monolayer MoS_2, offering intriguing possibilities for realizing interband tunnel FET with lower power dissipation[9]. To scale down the gate length, Desai et al. demonstrated a prototype of a junction-less MoS_2 transistor with a physical gate length of 1-nm using a metallic single-wall carbon nanotube as the gate electrode[10]. Ren et al. further decreased the gate length to sub-1 nm by designing side-wall 2D transistors gated with the edge of graphene[11]. Most of these advancements have focused on the development of n-type transistors. However, achieving programmable ambipolar operation within the same MoS_2 FET remains an elusive goal. The polarity of FET critically depends on injecting either electrons or holes into the semiconductor channel. Conventionally, metal-semiconductor interfaces determine polarity through Schottky barrier heights for electron and hole transport, where a small Schottky barrier height to conduction or valence band facilitates n-type or p-type behavior, respectively[12]. However, previously reported MoS_2 devices utilizing high work function metal palladium (Pd) contacts exhibit n-type instead of p-type behavior, usually ascribed to Fermi-level pinning (FLP) at the interface[13]. MoO_x nanoparticle/buffer layer with an ultrahigh work function potential (~6.1 eV) has been explored as contacts for efficient hole injection in ambipolar MoS_2 FETs[14,15]. Efforts have also been devoted to achieving ambipolar FET and tunable rectifying behavior in MoS_2 homojunction through chemical doping and MoS_2 heterostructures coupled with other materials such as carbon nanotube films[16]. Doping control by an electrostatic gate in MoS_2 FETs has provided significant opportunities. To date, hole transport in MoS_2 has been reported using insulator engineering (e.g., SiO_2[17]), albeit with limited tuning capability, via ionic electrolyte gating, which often induces electrochemical reactions[18–20], or van der Waals contact engineering[21]. A highly desirable alternative approach to reversible ambipolar MoS_2 FETs on the same chip without intrinsic/extrinsic doping or complex processing steps is sought.

The utilization of a ferroelectric gate has demonstrated its efficacy as a powerful tool for electrostatic modulation. On the one hand, ferroelectric polarization generates an intense electric field of GV/m, enabling substantial modulation of carrier concentration and band structure within the channel region[7,22–24]. On the other hand, ferroelectric hysteresis endows electronic devices with memory functionality that has found applications in neuromorphic devices[25–30] and reconfigurable lateral p-n junctions[23,24]. Herein, we propose a vertical tunneling ferroelectric FET (FeFET) in which the MoS_2/h-BN/metal tunnel junction rather than a single semiconductor is designed as a channel. The ambipolar behavior of MoS_2 is achieved by a ferroelectric electrostatic field, and the change of Fermi level within the MoS_2 electrode is read out through quantum tunneling currents across the atomic-thin h-BN layer. Since the direct quantum tunneling strength is extremely sensitive to the barrier shape that is co-defined by MoS_2 band alignments, the vertical tunneling FeFET exhibits a record-high ON/OFF ratio of up to 10^9. Through comparison among symmetric/asymmetric Schottky-contacted MoS_2-FeFETs and the vertical tunneling MoS_2-FeFET, the decisive role of electrode contact interface for electronic behaviors is reinforced. The large tunnel electroresistance through the Van der Waals junction by external ferroelectric polarization offers a platform as either a precise Fermi-level detection technique for physical research or a new block of memory communities for storage applications.

Results

Structure and electrical transport properties of vertical tunneling FeFET

We fabricated various MoS_2-based FETs featuring distinct contact interfaces. Organic ferroelectric poly (vinylidene fluoride) and trifluoroethylene (P(VDF-TrFE)) were employed as gate layers, with Al as the gate electrode. Graphene (Gr) layers are introduced at the large-area source electrode end to achieve ohmic contact[31,32]. h-BN layers are introduced at the Drain 1 end to establish a tunneling contact, while the Cr/Au electrode makes direct contact with the MoS_2 channel at the Drain 2 end. A novel ferroelectric memory with MoS_2/h-BN/metal tunnel junction as channel is prepared when Drain 1 is employed, referred to as vertical tunneling MoS_2-FeFET. An asymmetric Schottky-contacted MoS_2-FeFET is obtained when Drain 2 is utilized. The detailed device fabrication process is presented in the "Methods" section and Fig. S1. Figure 1a, b show schematics and optical images of the device, respectively. The h-BN and graphene are highlighted by black and blue dashed lines, respectively, while MoS_2, spanning the entire electrode, is labeled with an orange dashed line. The source electrode measures 5 µm in width, whereas the drain electrodes on both sides have a width of 2 µm. The boundaries among MoS_2, graphene, and h-BN were checked using the cross-sectional TEM technique. As shown in Fig. S2, both h-BN/MoS_2 and Gr/MoS_2 contacts show clear and sharp interfaces. The MoS_2 films are constituted by 3–4 layers with a thickness of ~2.5 nm. The BN films consist of 11–12 layers with a thickness of ~4 nm. The Gr films are made up of 13–14 layers with a thickness of ~4.5 nm. Figure 2c illustrates the Raman spectra of the MoS_2/h-BN and MoS_2/Gr structures at room temperature. The E_{2g} and A_{1g} characteristic peaks of 2H-MoS_2 are situated at 383.2 cm^{-1} and 407.5 cm^{-1}, respectively. The difference between E_{2g} and A_{1g} modes is 24.3 cm^{-1}, demonstrating that the exfoliated MoS_2 is multilayer[33]. The characteristic peak of h-BN is positioned at 1366.5 cm^{-1}. Additionally, the Raman characteristic G and 2D peaks of graphene are located at 1582 cm^{-1} and 2724 cm^{-1}, respectively. All the characteristic peaks of the heterostructures are in good agreement with the previous reports, implying that the sample is of high quality[34].

The ferroelectric gate layer of P(VDF-TrFE) is another key factor determining the device's performance. The P(VDF-TrFE) films on the Al electrode exhibit good flatness and homogeneity with a root mean square (RMS) roughness of 2.470 nm (Fig. S3a). The ferroelectric nature of the P(VDF-TrFE) thin films is confirmed by the butterfly-shaped amplitude loop and rectangular-shaped phase loop with 180° reversal (Fig. S3c), achieved by applying a stepwise voltage using piezoresponse force microscopy (PFM) tip (Fig. S3b). The reproducibility of ferroelectric domain switching is verified by the out-of-plane PFM images. The "ECNU"-shaped ferroelectric domain features were written by alternately applying +30 V and −30 V biases to the PFM tip while grounding the Al bottom electrode. A clear 180° phase contrast is observed between adjacent domains (Fig. 1d), with the amplitude values minimized at the domain walls (Fig. 1e). The ferroelectricity of the P(VDF-TrFE) thin film is further corroborated by the polarization versus voltage (P–V) hysteresis loops and polarization reversal-based peaks within the transient current curves of the Al/P(VDF-TrFE) (~280 nm)/Al capacitor (Fig. 2f). Multiple internal hysteresis loops can be obtained by gradually changing the amplitude of the scanning voltage (Fig. S3d).

Figures 1g and 1h present the transfer curves of asymmetric Schottky-contacted MoS_2-FeFET and vertical tunneling MoS_2-FeFET at $V_{DS} = \pm 0.3$ V on a semi-log scale, respectively. During the transfer curve measurement, the drain-to-source voltage (V_{DS}) remains constant while gate voltage (V_{Gate}) sweeps from −22 V to 22 V and subsequently retraces its path back to −22 V. For the asymmetric Schottky-contacted MoS_2-FeFET, it's evident that V_{DS} exerts a substantial influence on transfer characteristics. When V_{DS} is −0.3 V, bipolar behavior is observed. In contrast, at V_{DS} = 0.3 V, the device displays typical n-type

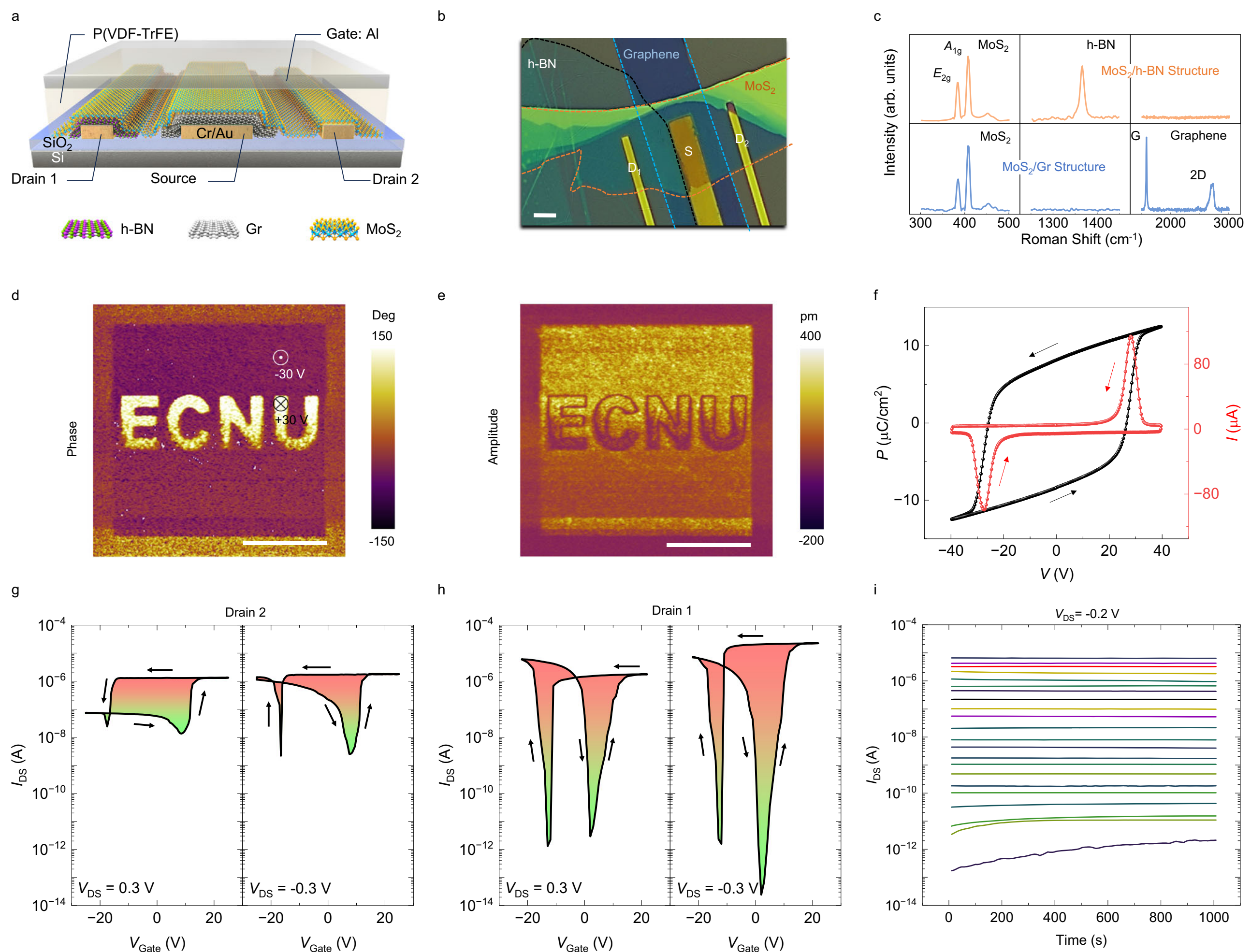

Fig. 1 | Device characterization. a Schematic of MoS_2-FeFET with P(VDF-TrFE) as ferroelectric gate, Gr/Au/Cr as Source, h-BN/Au/Cr as Drain 1, and Au/Cr as Drain 2. **b** Optical microscope photograph of the device. The red, black, and blue dashed lines outline MoS_2, h-BN, and Gr, respectively. Scale bar: 5 µm. **c** Raman spectra for MoS_2/h-BN and MoS_2/Gr heterostructures. **d**, **e** PFM phase (**d**) and amplitude (**e**) images of P(VDF-TrFE) film after writing an "ECNU" shape with a biased conductive tip. Scale bar: 4 µm. **f** Polarization versus voltage (*P*–*V*) and transient current versus voltage (*I*-*V*) curves measured for Al/P(VDF-TrFE)/Al capacitor. The test frequency is 100 Hz. **g**, **h** Transfer curves of asymmetric Schottky-contacted MoS_2-FeFET (**g**) and vertical tunneling FeFET (**h**) in a semi-log plot, measured at $V_{DS} = \pm 0.3$ V. **i** The retention characteristics of 22 intermediate conductance states in vertical tunneling MoS_2-FeFET that is measured at $V_{DS} = -0.2$ V.

characteristics. Additionally, the transfer curves exhibit clockwise and counterclockwise hysteresis loops for the hole and electron currents regime, respectively, emphasizing that ferroelectric switching serves as the dominant mechanism for resistive switching. The transfer curves of the vertical tunneling MoS_2-FeFET clearly reveal ambipolar features for both polarities of V_{DS}. Interestingly, when V_{DS} is positive, the device demonstrates a more pronounced p-type behavior, contrasting with the tendency of asymmetric Schottky-contacted MoS_2-FeFET, which shows n-type characteristics under positive V_{DS}. Moreover, the vertical tunneling MoS_2-FeFET achieves an ultrahigh current switching ON/OFF ratio of up to 10^9 (Fig. 2h) and realizes 22 distinct conductance states with minor variation over a period of 10^3 s except the gradual rising in the ultralow conductance state (Fig. 2i), indicating possible potential for robust multi-bit memory and neuromorphic computing applications.

The critical role of interface contacts on ambipolar behavior

Since the same MoS_2 flake was used in the asymmetric Schottky-contacted MoS_2-FeFET and vertical tunneling MoS_2-FeFET, the difference in electrical transport properties is reasonably attributed to the different interface contacts. To comprehensively understand the underlying reason for alteration between n-type unipolar and ambipolar behaviors in MoS_2-FETs, we also fabricated a symmetric Schottky-contacted MoS_2-FeFET using symmetric Cr/Au (50 nm) electrodes as shown in Fig. S4. The device features a similar channel to that of the asymmetric FeFETs. As shown in Fig. 2d, g, the transfer curves reveal a prototypical n-type unipolar FeFET at both $V_{DS} = -0.3$ V and $V_{DS} = 0.3$ V, aligning with prior observations in most MoS_2 FeFETs[7,28,29,35]. For clarity, the transfer curves of asymmetric Schottky-contacted MoS_2-FeFET and vertical tunneling FeFET at $V_{DS} = \pm 0.3$ V are presented in Fig. 2e, h and Fig. 2f, i, respectively. Evidently, the electrode contacts significantly influence the electronic properties of MoS_2-FeFETs, suggesting interfacial effects are paramount in governing device performance.

Figure 3 presents a series of color maps of transfer curves under different V_{DS} settings for MoS_2-FeFETs utilizing different contact configurations, with the data derived from Figs. S5–7. Specifically, Fig. 3a–c depict the process of ferroelectric polarization state persisting and gradually turning from downward to upward around negative coercive voltage (~ − 15 V) as V_{Gate} scans from +22 V to −22 V, while Fig. 3d–f reflect the reverse process with the polarization persisting and switching from upward to downward around positive coercive voltage (~15 V) as V_{Gate} sweeps from −22 V to +22 V. The two-dimensional color plot of I_{DS} for symmetric Schottky-contacted MoS_2-FeFET (Fig. 3a and Fig. 3d) vividly portrays the ON states occurring under both positive and negative V_{DS} in scenarios dominated by

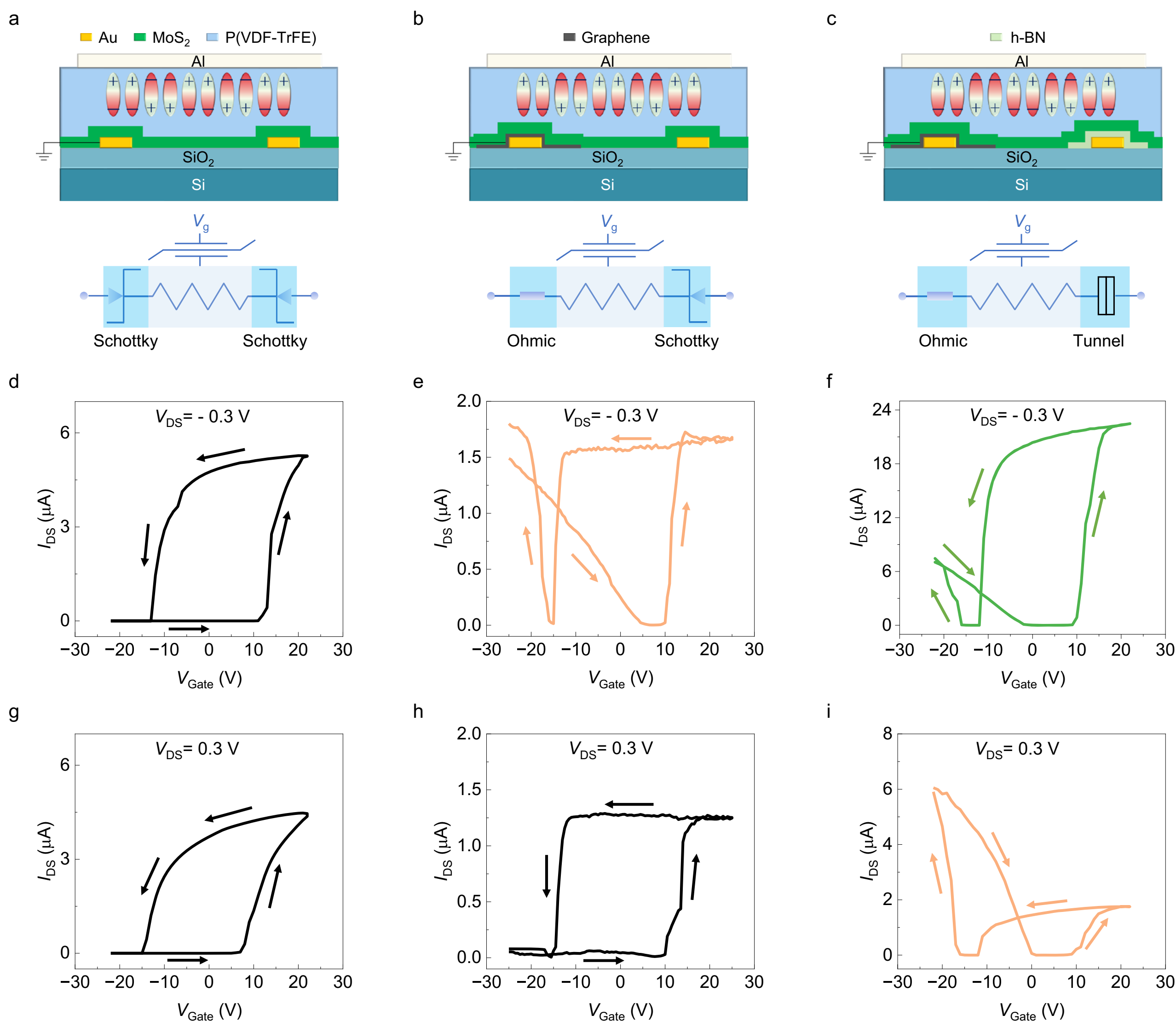

Fig. 2 | V_{DS}-dependent transfer curves in MoS_2-FeFETs with different contacts. **a**–**c** Schematics of symmetric Schottky-contacted MoS_2-FeFET (**a**), asymmetric Schottky-contacted MoS_2-FeFET (**b**), and vertical tunneling MoS_2-FeFET (**c**). **d**–**f** Transfer curves of symmetric Schottky-contacted MoS_2-FeFET (**d**), asymmetric Schottky-contacted MoS_2-FeFET (**e**) and vertical tunneling MoS_2-FeFET (**f**) in linear coordinates, measured at $V_{DS} = -0.3$ V. **g**–**i** Transfer curves of symmetric Schottky-contacted MoS_2-FeFET (**g**), asymmetric Schottky-contacted MoS_2-FeFET (**h**) and vertical tunneling MoS_2-FeFET (**i**) in linear coordinates, measured at $V_{DS} = 0.3$ V.

electron conduction, whereas the channel switches OFF when hole conduction prevails. In the case of asymmetric Schottky-contacted MoS_2-FeFET (Fig. 3b, e), it is discernible that once V_{DS} falls below a critical threshold value of −0.1 V, the device reverts to exhibiting ambipolar transfer characteristics. Above this threshold, the transfer curves display a typical n-type unipolar field effect. Moreover, the current profile exhibits symmetry in response to V_{DS} polarity in the positive V_{Gate} regime yet dissipates into asymmetry in the negative V_{Gate} range. The color mappings of the I_{DS} for vertical tunneling MoS_2-FeET (Fig. 3c, f) show a prominent ambipolar transfer behavior, with the ON state visible on both electron and hole regimes. An important observation here is the manifestation of opposite asymmetries in current values with respect to V_{DS} polarity. Specifically, the current is bigger at negative V_{DS} (Fig. 3c) in the electron conduction regime, while it is higher at positive V_{DS} (Fig. 3f) in the hole conduction regime. This differs from the behavior in an asymmetric Schottky-contacted MoS_2-FeFET with larger currents at negative V_{DS} (Fig. 3e) in the hole conduction regime.

To delve into the underlying mechanisms of our findings, hall measurements were performed on a MoS_2 flake that is covered by ferroelectric polymer films. The hall measurements provide information on carrier type and density, reflecting the influence of ferroelectric polarization on the energy band alignment of MoS_2. The dominant carrier of MoS_2 is electron with a density of $1.2 \times 10^{18}/cm^3$ for the pristine ferroelectric state, hole with a density of $6.7 \times 10^{15}/cm^3$ for the upward ferroelectric state, and electron with a density of $4.5 \times 10^{18}/cm^3$ for the downward ferroelectric state, respectively (Table S1). Based on the energy band model, the Femi level of MoS_2 nearly overlaps the conduction band edge for the downward polarization state and is 0.18-0.3 eV above the valence band edge for the upward polarization state, according well with previous reports[36]. Figure 4 plots the line cuts of the I_{DS}-V_{DS} profile along fixed $V_{Gate} = -3$ V from the black dashed lines marked in Fig. 3, along with their associated energy band diagrams. As V_{Gate} sweeps from positive to negative values, the ferroelectric polarization remains towards MoS_2 at $V_{Gate} = -3$ V. For symmetric Schottky-contacted MoS_2-FeFET, the currents are dominated by electrons injection from negatively-biased terminal (i.e., the Schottky junction in reverse-bias mode) into the MoS_2 channel, regardless of the polarity of V_{DS}. Given that MoS_2 is an inherent n-type semiconductor, the strong local electric field induced

https://doi.org/10.1038/s41467-024-54114-3

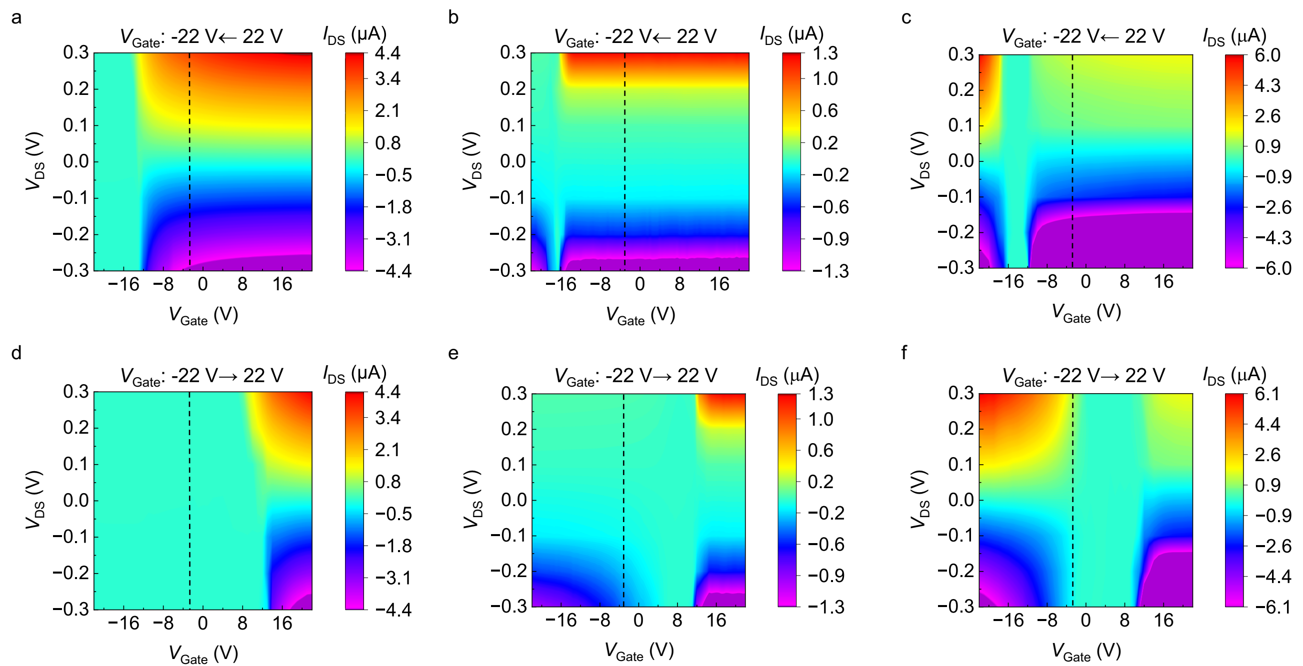

Fig. 3 | Color mapping of I_{DS} with evolution of V_{Gate} and V_{DS}. **a–c** Color mapping of transfer curves at different V_{DS} for symmetric Schottky-contacted MoS_2-FeFET (**a**), asymmetric Schottky-contacted MoS_2-FeFET (**b**), and vertical tunneling MoS_2-FeFET (**c**), with V_{Gate} sweeping from 22 V to −22 V. **d–f** Color mapping of transfer curves at different V_{DS} for symmetric Schottky-contacted MoS_2-FeFET (**d**), asymmetric Schottky-contacted MoS_2-FeFET (**e**), and vertical tunneling MoS_2-FeFET (**f**), with V_{Gate} sweeping from −22 V to 22 V.

by the downward ferroelectric polarization of P(VDF-TrFE) effectively prompts n-type (or highly n-type doping) behavior in MoS_2 and narrows Schottky barrier (upper left panel for negative V_{DS} and upper right panel for positive V_{DS} in Fig. 4a), thus vastly facilitating electron transport and resulting in a substantial current magnitude (lower panel in Fig. 4a). Conversely, upon reversing the sweeping direction of V_{Gate} from negative to positive values, the ferroelectric polarization points away from MoS_2 at $V_{Gate} = -3$ V. The electrons in MoS_2 are depleted, concurrently accompanied by hole accumulation, with the Fermi level approaching the top of the valence band and lightly p-type doping characteristic in MoS_2. Under these circumstances, holes become the primary charge carriers, and the currents are dominated by hole injection from a positively biased terminal (i.e., the Schottky junction in reverse-bias mode) into the MoS_2 channel. However, the lightly p-type doping gives a much wider hole Schottky barrier (upper left panel for negative V_{DS} and upper right panel for positive V_{DS} in Fig. 4d), yielding a considerably diminished current level (lower panel in Fig. 4d).

The carrier injection in asymmetric Schottky-contacted MoS_2-FeFET is determined by the Schottky barrier established at the MoS_2/Au interface on the drain side. In lower panel of Fig. 4b, we observe a bidirectional opening conductivity feature, with a remarkable current of 1.5 μA recorded at $V_{DS} = \pm 0.3$ V. This can be understood by the highly n-type doping under the downward polarization state where the Schottky barrier for electrons becomes so thin that enables uninhibited electron transmission under either positive or negative biasing (upper left panel for negative V_{DS} and upper right panel for positive V_{DS} in Fig. 4b). The I_{DS}-V_{DS} curve taken from Fig. 3e at $V_{Gate} = -3$ V demonstrates negative-pass behavior for upward polarization (lower panel in Fig. 4e). In this scenario, the negative (positive) V_{DS} would forward (backward) bias the hole Schottky barrier (upper left panel for negative V_{DS} and upper right panel for positive V_{DS} in Fig. 4e), rationalizing the rectifying trend of current curve (lower panel in Fig. 4e). Additionally, the current value of 0.35 μA at $V_{DS} = -0.3$ V in Fig. 4e is notably diminished compared to the corresponding value in Fig. 4b, in full agreement with the increased Schottky barrier width that effectively impedes hole conduction under upward polarization. More detailed information about the output curves of asymmetric Schottky-contacted FeFETs can be found in Fig. S8 and Fig. S9, clearly demonstrating full-pass, OFF to negative-pass transition during the V_{Gate} sweeping from +22 V to −22 V (Fig. S8) and reversed process (Fig. S9), respectively.

In the case of vertical tunneling MoS_2-FeFET, the carrier transport properties are governed by asymmetric Van der Waals MoS_2/h-BN/metal tunnel junction. According to Fermi's golden rule, the tunneling current is proportional to the density state at energy E in one electrode, the probability of state at E in the other electrode being empty, and the transfer matrix determining the transition probability between two electrodes. When the ferroelectric polarization aligns towards MoS_2, electron tunneling through ultrathin h-BN dielectrics becomes the dominant transport mechanism. A negative V_{DS} encourages a substantial electron flow from the metal to MoS_2 (upper left panel in Fig. 4c), engendering a large conduction current. While for a positive V_{DS}, tunneling of electrons from the semiconductor to the metal (upper right panel in Fig. 4c) is significantly impeded by the disparity in electron concentrations, i.e., a lower concentration of electrons in the semiconductor relative to the metal electrode, yielding minimal current flow. Consequently, the output curves behave as typical negative-pass rectification (lower panel in Fig. 4c). Of particular interest is the observation that the diode behavior is inverted by switching the ferroelectric polarization direction (lower panel in Fig. 4f). With the ferroelectric polarization pointing away from MoS_2, hole tunneling plays a leading role. When V_{DS} is positive, a surge in holes tunneling from the electrode to MoS_2 (upper right panel in Fig. 4f) significantly boosts the current. On the contrary, under negative V_{DS} conditions, the tunneling current of holes from the semiconductor into the electrode (upper left panel in Fig. 4f) is drastically curtailed due to the difference in the density of states for holes between MoS_2 and metal electrodes. Upon switching the ferroelectric polarization, the output levels of vertical tunneling MoS_2-FeFET demonstrate negative-pass, OFF to full-pass transition during the V_{Gate} sweeping from +22 V to −22 V (Fig. S10) and full-pass, positive-pass, OFF to negative-pass transition during the V_{Gate}

https://doi.org/10.1038/s41467-024-54114-3

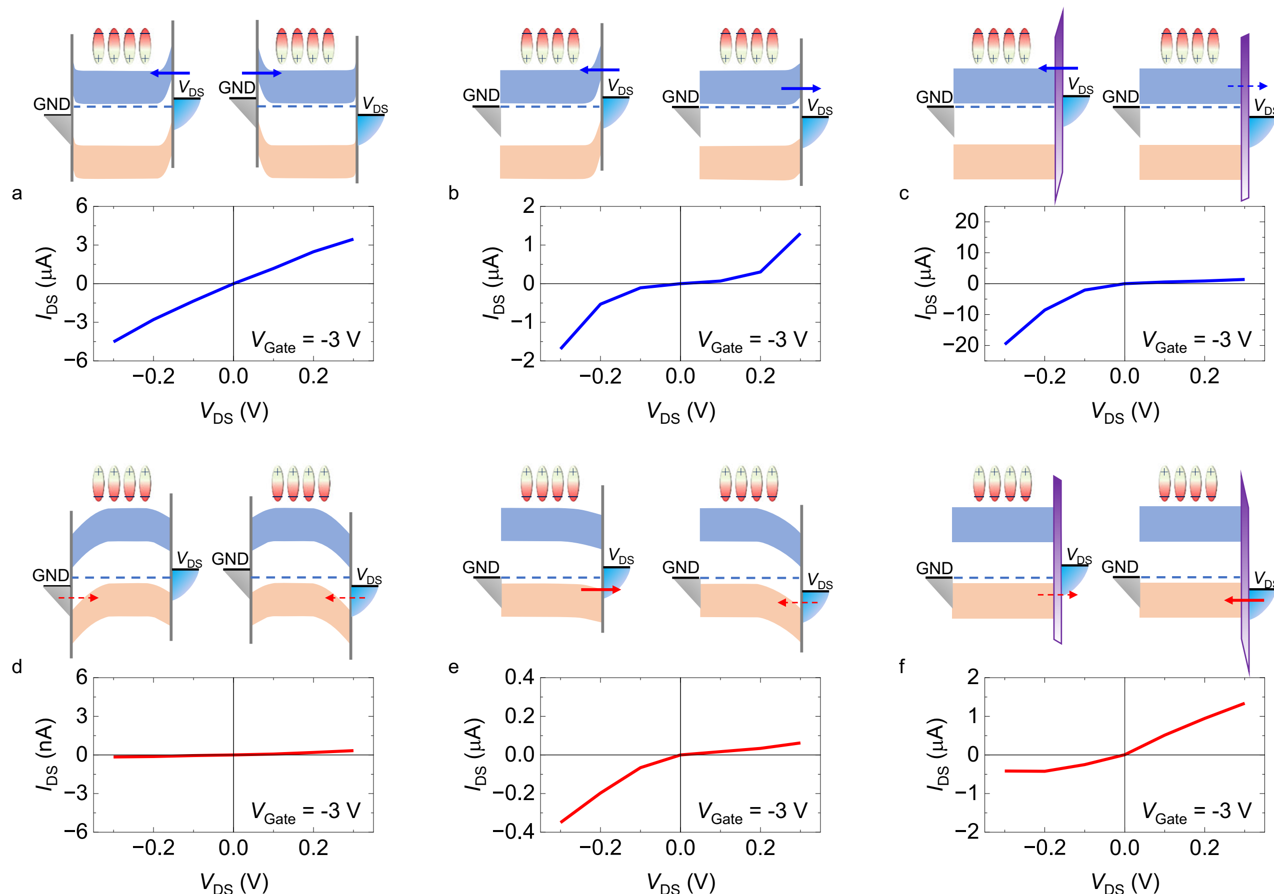

Fig. 4 | Polarization-dependent output curves in MoS_2-FeFETs with different contacts. a–c Schematic band alignments and output curves of symmetric Schottky-contacted MoS_2-FeFET (**a**), asymmetric Schottky-contacted MoS_2-FeFET (**b**) and vertical tunneling MoS_2-FeFET (**c**) for downward ferroelectric polarization state. **d–f** Schematic band alignments and output curves of symmetric Schottky-contacted MoS_2-FeFET (**d**), asymmetric Schottky-contacted MoS_2-FeFET (**e**) and vertical tunneling MoS_2-FeFET (**f**) for upward ferroelectric polarization state. The output curves in **a–f** along fixed gate voltage correspond to the black dashed lines in Fig. 3a–f, respectively.

sweeping from −22 V to +22 V (Fig. S11). This intriguing polarity switch underscores the profound influence of ferroelectric polarization and tunneling effect on the device's electronic performance.

The simple band alignment model in Fig.4 clarifies the output curves of MoS_2-FeFETs with all-kind contacts very well. This model also effectively elucidates the striking difference in polarity behavior between the transfer curves of asymmetric Schottky-contacted MoS_2-FeFET and vertical tunneling MoS_2-FeFET. In asymmetric Schottky-contacted FeFETs, despite that a negative V_{DS} would reverse-bias Schottky barrier for electrons and forward-bias Schottky barrier for holes, appreciable current can still be observed even for downward polarization due to the relatively narrow width of the electron Schottky barrier, resulting in ambipolar behavior at $V_{DS} = -0.3$ V. By contrast, a positive V_{DS} enhances electron flow by forward-biasing electron Schottky barrier and simultaneously suppresses hole conduction through reverse-biasing hole barrier, causing the transfer curve to exhibit the behavior akin to that of an n-type FeFET. Regarding tunnel-contacted counterpart, because the carriers' density in the metal is much higher than that in the MoS_2, at $V_{DS} = 0.3$ V, the current for electrons tunneling from MoS_2 to the electrode is significantly diminished relative to the tunneling current of holes in the reverse path, thereby tilting the transfer curve towards more pronounced p-type characteristic. Conversely, when V_{DS} is −0.3 V, the situation is reversed, with the n-type behavior being more evident due to the dominant tunneling of electrons from the electrode into the MoS_2 channel. This dual nature of the transfer curves highlights the effectiveness of the tunneling junction as a channel and accentuates the pivotal role of V_{DS} polarity in dictating the operative regime of the semiconductor, thereby dynamically steering the device between n-type and p-type conduction modes.

The mechanism for enhanced switching ratio of vertical tunneling FeFET

The transfer curve of vertical tunneling MoS_2-FeFET depicted in Fig. 1h discloses an impressive ON/OFF ratio reaching up to 10^9 when V_{DS} is set as −0.3 V, more than five orders of magnitude larger than that of asymmetric Schottky-contacted MoS_2-FeFET. The band alignments for the ON-state with the Fermi level of MoS_2 residing near the conduction band (left panel) and OFF-state with the Fermi level of MoS_2 positioned in the middle of the bandgap (right panel) are shown in Fig. 5a, b, corresponding to asymmetric Schottky-contacted MoS_2-FeFET and vertical tunneling MoS_2-FeFET, respectively. As the thickness of two-dimensional semiconductors shrinks to the nanoscale or even atomic level, challenges arise from large OFF-state current, consuming additional standby power and suppressing the switching ratio. Inserting insulator layers, such as Al_2O_3 and h-BN, has been validated to be an effective strategy to mitigate OFF-state current[37,38]. However, this mitigation often comes at the cost of reducing the ON-state current. Intriguingly, in the case of our vertical tunneling MoS_2-FeFET, the insertion of an h-BN interlayer between the MoS_2 and metal electrode results in a uniform band potential across the entire MoS_2, leaving only a very thin tunneling barrier[21]. The tunneling injection intensity of

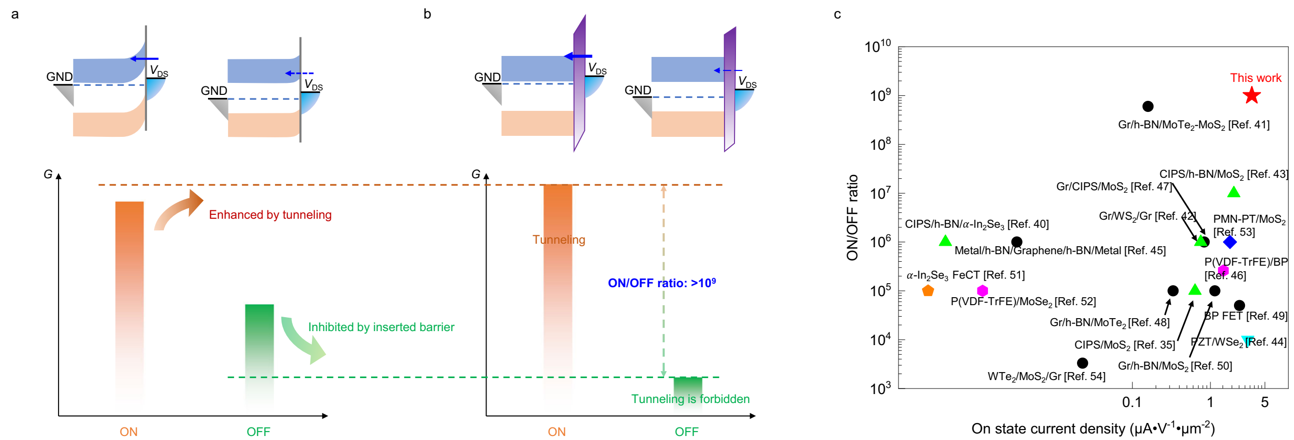

Fig. 5 | The mechanism for enhanced switching ratio of vertical tunneling MoS_2-FeFET. a, b The energy band alignments for ON-state and OFF-state of asymmetric Schottky-contacted MoS_2-FeFET (**a**) and vertical tunneling MoS_2-FeFET (**b**). Insets highlight the ON/OFF ratio of MoS_2-FeFETs. **c** Benchmark plot of switching ratio and ON-state current density per unit area per volt for vertical tunneling MoS_2-FeFET compared with previously reported 2D FETs[35,40–54].

carriers passing through this thin tunneling layer is significantly greater than the injection intensity across the Schottky barrier of a metal/MoS_2 contact. This accords well with previous report[39]. Thus, here the insertion of tunnel h-BN layer achieves a dual advantage: it suppresses the OFF-state current while simultaneously boosting the ON-state current, thereby significantly enhancing the switching ratio.

For a comprehensive assessment of FET performance, a comparison chart in Fig. 5c summarizes the ON/OFF ratio and ON-state current density per unit area extracted from previous studies[35,40–54]. A significant ON/OFF ratio is pivotal for achieving low-power consumption and high-density integration of devices, while a high ON-state current enables faster access speeds. Our novel ferroelectric memory, utilizing a vertical tunnel junction channel, showcases notable performance characteristics compared to other 2D channel FETs, including a high ON/OFF ratio and a robust ON-state current density. Such features lay the groundwork for novel advancements in future memory and logic devices.

Memory characteristics of vertical tunneling FeFET

As a potential memory device, key memory characteristics such as operating speed, energy consumption, and endurance behavior are tested for vertical tunneling MoS_2-FeFETs. The device is programmed to OFF states by applying constant negative V_{Gate} pulses (−14 V, 5 ms) and to ON states by applying positive V_{Gate} pulses with amplitudes ranging from 14 V to 31 V and pulse widths between 1 ms and 500 ns. Each programming voltage is followed by a constant $V_d = -0.2$ V to verify the conductance state of the Van der Waals junction. As shown in Fig. 6a, despite the increasing voltage amplitude, the ON/OFF ratio gradually decays with the decrease of operating voltage pulse width. The vertical tunneling MoS_2-FeFET achieves a switching speed as fast as 500 ns by a 31 V pulse, while still maintaining an ON/OFF ratio of more than 10^4.

The energy consumption is calculated using the formula $E = UIt$, where U, I, and t are the operating voltage amplitude, the leakage current, and the operating speed, respectively. The gate leakage current of the vertical tunneling MoS_2-FeFETs is at the picoampere level, as seen in Fig. S12. The energy consumption for opening an ON/OFF ratio of more than 10^4 by the 22 V (1 μs) and 31 V (500 ns) operations is ~0.22 fJ and ~0.16 fJ, respectively. Note that this is the record low energy consumption of memory devices to the best of our knowledge. The cycling tests are conducted to check the endurance behavior of vertical tunneling MoS_2-FeFETs. To avoid the disturbance of the joule heating effect by high channel currents during the cycling tests, a low

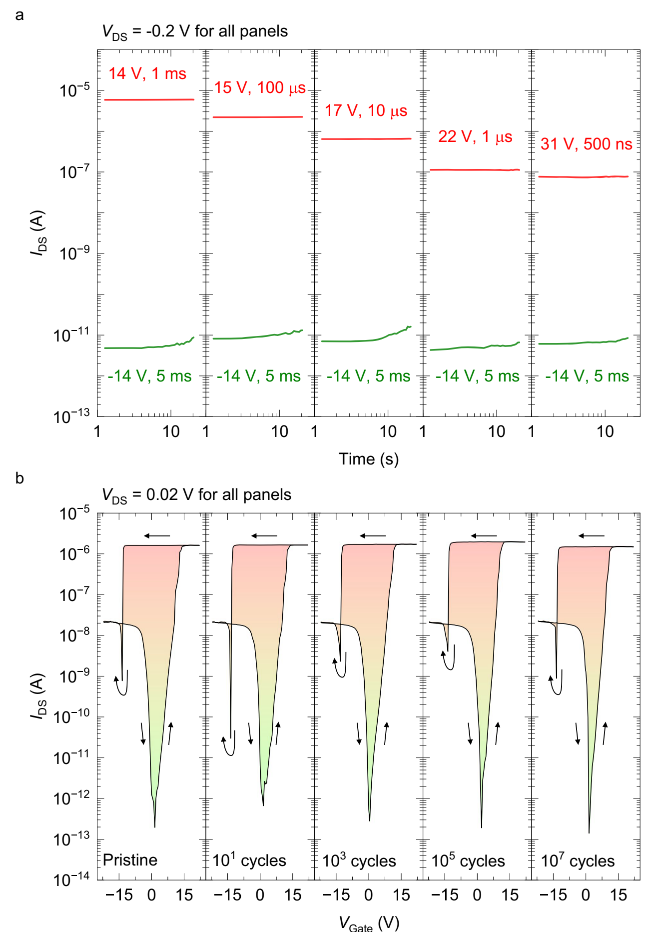

Fig. 6 | The switching speed and endurance behavior of vertical tunneling MoS_2-FeFET. a The evolution of I_{DS} with time after programming the device using constant negative V_{Gate} pulses (−14 V, 5 ms) (green lines) and positive V_{Gate} pulses (14 V, 1 ms; 15 V, 100 μs; 17 V, 10 μs; 22 V, 1 μs and 31 V, 500 ns) (red lines), respectively. The $V_{DS} = -0.2$ V for all panels. **b** The evolution of transfer curves with the cycles (pristine, 10, 10^3, 10^5, and 10^7) of voltage triangle wave with an amplitude of 30 V and frequency of 10 kHz for a vertical tunneling MoS_2-FeFET. The $V_{DS} = 0.02$ V for all panels.

V_{DS} of only 0.02 V is used. The transfer curve is checked after 10, 10^3, 10^5, and 10^7 cycles of voltage triangle wave with an amplitude of 30 V and frequency of 10 kHz and compared with the pristine one (Fig. 6b). These transfer curves, characterized by a huge ON/OFF ratio of ~7 orders with the ultralow V_{DS} = 0.02 V, exhibits minimal variation during all cycling tests, implying that the device still works well after 10^7 cycles.

A lower operating voltage is preferable from the view of practical application. This can be obtained by reducing the thickness of the ferroelectric layer in the vertical tunneling MoS_2-FeFET device. As shown in Fig. S13, the operating voltage decreases from 20 V for the device with a 200 nm-thick ferroelectric layer to 10 V for the device with a 100 nm-thick ferroelectric layer. It should be noted that the voltage scaling is not always linear with decreasing thickness when the thickness approaches nanoscale. The interfacial strain and electrostatic boundary conditions may play an increasingly dominant role and can even increase the fields required for switching. Further work is needed to optimize the ultrathin and high-quality ferroelectric films to achieve operating voltages low enough for compatibility with mature complementary metal-oxide-semiconductor (CMOS) technology. The ultrathin hafnium-based ferroelectrics, present promising alternatives that warrant further exploration in this novel memory structure.

It is worth comparing the vertical tunneling FeFET with the Ferroelectric Tunneling Junction (FTJ), which takes advantage of the direct quantum tunneling effect through the ferroelectric layer. An FTJ device typically requires the ferroelectric layer to be only a few nanometers. However, the coercive electric field in nanoscale ferroelectric thin films is significantly higher than that in bulky films, suffering from poor fatigue performance in FTJs ($<10^6$ cycles)[55]. Unlike FTJs, the ferroelectric layer in vertical tunneling FeFETs does not function as a tunneling layer but as a third control terminal, that is, the tunnel electroresistance through the below Van der Waals junction is achieved by modulating the Femi level of 2D semiconductor electrode by an external ferroelectric gate. This removes the thickness constraint imposed by quantum tunneling, effectively mitigating the fatigue issues associated with FTJs. As shown in Fig. 6b, the vertical tunneling MoS_2-FeFET still works well after 10^7 cycles. Besides, the leakage currents in a vertical tunneling FeFET that pass through thick and insulative ferroelectric gates are much lower than the inevitable tunneling currents in FTJ, pioneering energy consumption as low as 0.16 fJ per operation.

In summary, we have demonstrated a novel device architecture, a vertical tunneling FeFET in which the Van der Waals MoS_2/h-BN/metal tunnel junction is the channel. The Fermi level of MoS_2 was bipolarly tuned by ferroelectric domains and can be sensitively detected by the direct quantum tunneling strength across the junction. The device incorporating ~4 nm h-BN tunneling layer shows not only an ultralow OFF-state current but also a high ON-state current, yielding a striking ON/OFF ratio up to 10^9. It requires only 0.16 fJ of energy to achieve an ON/OFF ratio greater than 10^4. This ingeniously devised structure effectively exhibits ambipolar behavior and gate-tunable operation states of output level, including positive-pass, OFF, negative-pass, and full-pass modes. A free-moving band alignment model is powerful enough to elucidate the decisive role of the electrode contact interface for all these electrical properties. This work paves the way for future applications in gate-tunable logic devices adopting 2D semiconducting as the electrode for tunnel junction channels.

Methods

Device fabrication

Firstly, the electrode patterning was completed on a silicon wafer with a 300 nm-thick SiO_2 layer through electron-beam lithography. Cr/Au (10/50 nm) was then deposited through thermal evaporation. The h-BN, MoS_2, and graphene flakes were directly exfoliated into Polydimethylsiloxane (PDMS) with Scotch tape from single crystals purchased from HQ Graphene, Netherlands. The h-BN flake on the PDMS stamp was first stuck on a silicon wafer and picked up with polyvinyl alcohol (PVA). The h-BN flake on the PVA stamp was inverted and aligned onto Drain 1 using a micro-manipulator, followed by immersion of the sample in deionized water for 2 h to remove the PVA. Graphene from PDMS was transferred onto the Source terminal to form Ohmic contact. The MoS_2 flake on PDMS, covering Drain 1, Drain 2 and Source, was transferred on top of the device. Next, P(VDF-TrFE) (70:30 in mole ratio) was spin-coated as the gate dielectric layer, which was thermally annealed at 135 °C for 4 h to promote the formation of ferroelectric β-phase. Finally, 50 nm thick Al electrodes were prepared by thermal evaporation to complete the gate electrode.

Characterization method

Raman spectra were measured using a Raman system (Renishaw inVia) with an excitation wavelength of 532 nm. Transmission electron microscopy (TEM) analysis was conducted using a JEM-2100F field emission TEM (JEOL, Tokyo, Japan). P–V hysteresis loops of P(VDF-TrFE) were tested using a ferroelectric analyzer (TF Analyzer 3000). Piezoelectric force microscopy (Asylum Research Cypher) was applied to confirm the ferroelectricity of P(VDF-TrFE) films. The electrical properties of the devices prepared in this paper were measured, unless noted otherwise, under ambient conditions using a Keithley 4200A-SCS parameter analyzer with remote preamplifiers. The Hall effect measurements of MoS_2 were performed with the Linseis HCS 1 system.

Data availability

The data that support the findings of this study are available from the corresponding author upon reasonable request.

Code availability

The codes that support the findings of this study are available from the corresponding author upon reasonable request.

References

1. Jacob, A. P. et al. Scaling challenges for advanced CMOS devices. *Int. J. High. Speed Electron. Syst.* **26**, 1740001 (2017).
2. Kim, K. S. et al. The future of two-dimensional semiconductors beyond Moore's law. *Nat. Nanotechnol.* **19**, 895–906 (2024).
3. Das, S. et al. Transistors based on two-dimensional materials for future integrated circuits. *Nat. Electron.* **4**, 786–799 (2021).
4. Akinwande, D. et al. Graphene and two-dimensional materials for silicon technology. *Nature* **573**, 507–518 (2019).
5. Miao, J. S. et al. Heterojunction tunnel triodes based on two-dimensional metal selenide and three-dimensional silicon. *Nat. Electron.* **5**, 744–751 (2022).
6. Manzeli, S., Ovchinnikov, D., Pasquier, D., Yazyev, O. V. & Kis, A. 2D transition metal dichalcogenides. *Nat. Rev. Mater.* **2**, 17033 (2017).
7. Wang, X. D. et al. Ultrasensitive and broadband MoS_2 photodetector driven by ferroelectrics. *Adv. Mater.* **27**, 6575–6581 (2015).
8. Li, T. X. et al. Reconfigurable, non-volatile neuromorphic photovoltaics. *Nat. Nanotechnol.* **18**, 1303–1310 (2023).
9. Radisavljevic, B., Radenovic, A., Brivio, J., Giacometti, V. & Kis, A. Single-layer MoS_2 transistors. *Nat. Nanotechnol.* **6**, 147–150 (2011).
10. Desai, S. B. et al. MoS_2 transistors with 1-nanometer gate lengths. *Science* **354**, 99–102 (2016).
11. Wu, F. et al. Vertical MoS_2 transistors with sub-1-nm gate lengths. *Nature* **603**, 259 (2022).
12. Sun, X. X. et al. Contact and injection engineering for low SS reconfigurable FETs and high gain complementary inverters. *Sci. Bull.* **65**, 2007–2013 (2020).
13. Kim, C. et al. Fermi level pinning at electrical metal contacts of monolayer molybdenum dichalcogenides. *ACS Nano* **11**, 1588–1596 (2017).

14. Chuang, S. et al. MoS_2 P-type transistors and diodes enabled by high work function MoO_x contacts. *Nano Lett.* **14**, 1337–1342 (2014).
15. Choi, J. H. et al. Ambipolar behavior in MoS_2 field effect transistors by using catalytic oxidation. *Appl. Phys. Lett.* **109**, 183102 (2016).
16. Jariwala, D. et al. Gate-tunable carbon nanotube-MoS_2 heterojunction p-n diode. *Proc. Natl Acad. Sci. USA* **110**, 18076–18080 (2013).
17. Bao, W. Z., Cai, X. H., Kim, D., Sridhara, K. & Fuhrer, M. S. High mobility ambipolar MoS_2 field-effect transistors: substrate and dielectric effects. *Appl. Phys. Lett.* **102**, 042104 (2013).
18. Zhang, Y. J., Ye, J. T., Matsuhashi, Y. & Iwasa, Y. Ambipolar MoS_2 thin flake transistors. *Nano Lett.* **12**, 1136–1140 (2012).
19. Zhang, Y. J., Ye, J. T., Yornogida, Y., Takenobu, T. & Iwasa, Y. Formation of a stable *p-n* junction in a liquid-gated MoS_2 ambipolar transistor. *Nano Lett.* **13**, 3023–3028 (2013).
20. Ponomarev, E., Gutiérrez-Lezama, I., Ubrig, N. & Morpurgo, A. F. Ambipolar light-emitting transistors on chemical vapor deposited monolayer MoS_2. *Nano Lett.* **15**, 8289–8294 (2015).
21. Li, X. X. et al. Gate-controlled reversible rectifying behaviour in tunnel contacted atomically-thin MoS_2 transistor. *Nat. Commun.* **8**, 970 (2017).
22. Sun, Y. X. et al. Ambipolar MoS_2 field effect transistors with negative photoconductivity and high responsivity using an ultrathin epitaxial ferroelectric gate. *Adv. Funct. Mater.* **34**, 2402185 (2024).
23. Lv, L. et al. Reconfigurable two-dimensional optoelectronic devices enabled by local ferroelectric polarization. *Nat. Commun.* **10**, 3331 (2019).
24. Wu, G. J. et al. Programmable transition metal dichalcogenide homojunctions controlled by nonvolatile ferroelectric domains. *Nat. Electron.* **3**, 43–50 (2020).
25. Berdan, R. et al. Low-power linear computation using nonlinear ferroelectric tunnel junction memristors. *Nat. Electron.* **3**, 259–266 (2020).
26. Ning, H. K. et al. An in-memory computing architecture based on a duplex two-dimensional material structure for in situ machine learning. *Nat. Nanotechnol.* **18**, 493–500 (2023).
27. Wu, G. J. et al. Ferroelectric-defined reconfigurable homojunctions for in-memory sensing and computing. *Nat. Mater.* **22**, 1499–1506 (2023).
28. Tian, B. B. et al. A robust artificial synapse based on organic ferroelectric polymer. *Adv. Electron. Mater.* **5**, 1800600 (2019).
29. Yan, M. G. et al. Ferroelectric synaptic transistor network for associative memory. *Adv. Electron. Mater.* **7**, 2001276 (2021).
30. Feng, G. D. et al. A ferroelectric fin diode for robust non-volatile memory. *Nat. Commun.* **15**, 513 (2024).
31. Liu, Y. et al. Toward barrier free contact to molybdenum disulfide using graphene electrodes. *Nano Lett.* **15**, 3030–3034 (2015).
32. Chee, S. S. et al. Lowering the Schottky barrier height by graphene/Ag electrodes for high-mobility MoS_2 field-effect transistors. *Adv. Mater.* **31**, 1804422 (2019).
33. Lee, C. et al. Anomalous lattice vibrations of single- and few-layer MoS_2. *ACS Nano* **4**, 2695–2700 (2010).
34. Cong, X., Liu, X. L., Lin, M. L. & Tan, P. H. Application of Raman spectroscopy to probe fundamental properties of two-dimensional materials. *npj 2d Mater. Appl.* **4**, 13 (2020).
35. Si, M. W., Liao, P. Y., Qiu, G., Duan, Y. Q. & Ye, P. D. D. Ferroelectric field-effect transistors based on MoS_2 and $CuInP_2S_6$ two-dimensional van der Waals heterostructure. *ACS Nano* **12**, 6700–6705 (2018).
36. Sun, X. et al. Measuring band modulation of MoS_2 with ferroelectric gates. *Nano Lett.* **23**, 2114 (2023).
37. Si, M. W. et al. Asymmetric metal/α-In_2Se_3/Si crossbar ferroelectric semiconductor junction. *ACS Nano* **15**, 5689–5695 (2021).
38. Liu, X. L. et al. Ultralow off-state current and multilevel resistance state in Van der Waals heterostructure memristors. *Adv. Funct. Mater.* **34**, 2309642 (2024).
39. Wang, J. L. et al. High mobility MoS_2 transistor with low Schottky barrier contact by using atomic thick h-BN as a tunneling layer. *Adv. Mater.* **28**, 8302–8308 (2016).
40. Baek, S. et al. Ferroelectric field-effect-transistor integrated with ferroelectrics heterostructure. *Adv. Sci.* **9**, 2200566 (2022).
41. Cheng, R. Q. et al. High-performance, multifunctional devices based on asymmetric van der Waals heterostructures. *Nat. Electron.* **1**, 356–361 (2018).
42. Georgiou, T. et al. Vertical field-effect transistor based on graphene-WS_2 heterostructures for flexible and transparent electronics. *Nat. Nanotechnol.* **8**, 100–103 (2013).
43. Huang, W. H. et al. Gate-coupling-enabled robust hysteresis for nonvolatile memory and programmable rectifier in Van der Waals ferroelectric heterojunctions. *Adv. Mater.* **32**, 1908040 (2020).
44. Ko, C. et al. Ferroelectrically gated atomically thin transition-metal dichalcogenides as nonvolatile memory. *Adv. Mater.* **28**, 2923–2930 (2016).
45. Lee, J. H. et al. Semiconductor-less vertical transistor with I_{ON}/I_{OFF} of 10^6. *Nat. Commun.* **12**, 1000 (2021).
46. Lee, Y. T. et al. Nonvolatile ferroelectric memory circuit using black phosphorus nanosheet-based field-effect transistors with P(VDF-TrFE) polymer. *ACS Nano* **9**, 10394–10401 (2015).
47. Liaqat, A. et al. An all two-dimensional vertical heterostructure graphene/$CuInP_2S_6$/MoS_2 for negative capacitance field effect transistor. *Nanotechnology* **33**, 125703 (2022).
48. Sasaki, T. et al. Understanding the memory window overestimation of 2D materials based floating gate type memory devices by measuring floating gate voltage. *Small* **16**, 2004907 (2020).
49. Tian, H. et al. A dynamically reconfigurable ambipolar black phosphorus memory device. *ACS Nano* **10**, 10428–10435 (2016).
50. Vu, Q. A. et al. Two-terminal floating-gate memory with van der Waals heterostructures for ultrahigh on/off ratio. *Nat. Commun.* **7**, 12725 (2016).
51. Wang, S. Y. et al. Two-dimensional ferroelectric channel transistors integrating ultra-fast memory and neural computing. *Nat. Commun.* **12**, 53 (2021).
52. Wang, X. D. et al. Ferroelectric FET for nonvolatile memory application with two-dimensional $MoSe_2$ channels. *2D Mater.* **4**, 025036 (2017).
53. Xu, L. P. et al. Ferroelectric-modulated MoS_2 field-effect transistors as multilevel nonvolatile memory. *ACS Appl. Mater. Interfaces* **12**, 44902–44911 (2020).
54. Zhou, Y. Q. et al. Vertical nonvolatile Schottky-barrier-field-effect transistor with self-gating semimetal contact. *Adv. Funct. Mater.* **33**, 2213254 (2023).
55. Wen, Z. & Wu, D. Ferroelectric tunnel junctions: modulations on the potential barrier. *Adv. Mater.* **32**, 1904123 (2019).

Acknowledgements

Thank fundings of the National Natural Science Foundation of China (No. T2222025, 62474065, 62174053, and 12134003), the National Key Research and Development Program of China (No. 2021YFA1200700), Natural Science Foundation of Chongqing (CSTB2024NSCQ-JQX0005), Shanghai Science and Technology Innovation Action Plan (No. 21JC1402000 and 21520714100) and the Fundamental Research Funds for the Central Universities.

Author contributions

B.T. and Q.Z. conceived the concept and supervised the research. Y.L., Z.F., S.L., M.Z., and G.F. fabricated the devices. G.F., B.T., Y.L., and C.Q. performed the electrical measurements. L.C. and S.H. performed piezoresponse force microscopy measurements. H.W. and K.Q. performed the cross-sectional transmission electron microscopy measurements. Y.L., Y.X., and G.F. sketched the structure of the devices. B.T., Q.Z., K.Q., C.Y., F.Y., C.D., and J.C. advised on the experiments and data analysis.

Q.Z., G.F., Y.L., and B.T. co-write the manuscript. All authors discussed the results and revised the manuscript.

Competing interests

The authors declare no competing interests.

Additional information

Supplementary information The online version contains supplementary material available at https://doi.org/10.1038/s41467-024-54114-3.

Correspondence and requests for materials should be addressed to Qiuxiang Zhu or Bobo Tian.

Peer review information *Nature Communications* thanks Linfeng Sun, Qiang Zheng and the other anonymous reviewer(s) for their contribution to the peer review of this work. A peer review file is available.

Reprints and permissions information is available at http://www.nature.com/reprints

Publisher's note Springer Nature remains neutral with regard to jurisdictional claims in published maps and institutional affiliations.

Open Access This article is licensed under a Creative Commons Attribution-NonCommercial-NoDerivatives 4.0 International License, which permits any non-commercial use, sharing, distribution and reproduction in any medium or format, as long as you give appropriate credit to the original author(s) and the source, provide a link to the Creative Commons licence, and indicate if you modified the licensed material. You do not have permission under this licence to share adapted material derived from this article or parts of it. The images or other third party material in this article are included in the article's Creative Commons licence, unless indicated otherwise in a credit line to the material. If material is not included in the article's Creative Commons licence and your intended use is not permitted by statutory regulation or exceeds the permitted use, you will need to obtain permission directly from the copyright holder. To view a copy of this licence, visit http://creativecommons.org/licenses/by-nc-nd/4.0/.

© The Author(s) 2024